Effect of Annealing on Structural and Thermodynamic Properties of ThSiO4-ErPO4 Xenotime Solid Solution

A. Shelyug, M. Rafiuddin, Adel Mesbah, Nicolas Clavier, Stephanie
Szenknect, Nicolas Dacheux, X. Guo, A. Navrotsky

Effect of annealing on structural and thermodynamic properties of ThSiO$_4$-ErPO$_4$ xenotime solid solution

Anna Shelyug[1], Mohamed Ruwaid Rafiuddin[2], Adel Mesbah[2,3], Nicolas Clavier[2], Stéphanie Szenknect[2], Nicolas Dacheux[2], Xiaofeng Guo[4], Alexandra Navrotsky[5]*

[1]Institute of Solid State Chemistry, Yekaterinburg 620990, Russia

[2]ICSM, Univ Montpellier, CNRS, CEA, ENSCM, Site de Marcoule, Bagnols-sur-Cèze, France

[3]Univ Lyon, Université Lyon 1, Institut de Recherches sur la Catalyse et l'Environnement de Lyon, IRCELYON, UMR5256, CNRS, 2 Avenue Albert Einstein, 69626, Villeurbanne Cedex, France

[4]Department of Chemistry and Alexandra Navrotsky Institute for Experimental Thermodynamics, Washington State University, Pullman, WA 99164, USA

[5]School of Molecular Sciences a Center for Materials of the Universe, Arizona State University, Tempe, AZ 85287, USA

*Corresponding author: Alexandra Navrotsky alexandra.navrotsky@asu.edu

ABSTRACT

The effect of annealing on structural and thermochemical properties of the thorite-xenotime solid solution Th$_{1-x}$Er$_x$(SiO$_4$)$_{1-x}$(PO$_4$)$_x$ was assessed. The samples synthesized at low temperatures and stored at room temperature for two years retained their tetragonal structure. This structure was also maintained after heating to 1100 °C. During annealing, the structure lost water and exsolved some thorianite phase. The thermodynamic parameters did not change much after annealing, suggesting that xenotime was not a low temperature metastable phase but rather a stable structure able to withstand elevated temperatures regardless of thorium content. The solid solution exhibited subregular behavior with the Margules function W(x) = (73.1 ± 20.1) – (125.7 ± 49.8)·x.

1. INTRODUCTION

Monazite (REPO$_4$; RE = La to Gd), xenotime (REPO$_4$; RE = Tb to Lu and Y), and zircon (MSiO$_4$; M = Zr, Hf, Th, U) are widespread naturally occurring minerals [1–6] found in granitic and metamorphic rocks.[7–11] These minerals offer great compositional flexibility and can accommodate a wide range of combinations of rare earth elements (RE), natural actinides (AN = U and Th), and several anionic species within their crystal structure. For the geochemical community, owing to the presence of actinides (U, Th), associated daughter elements (Pb) and their high chemical durability, these minerals are often used for geochronology applications (dating methods).[12–20] The ability of these minerals to host various types of cations draws interest for nuclear waste management.[1,21–27] As a result, these materials have been proposed as a ceramic waste form for the disposal of minor actinides or plutonium resulting from dismantled nuclear weapons and reprocessing of spent nuclear fuel.[28,29] Both, REPO$_4$ and MSiO$_4$ matrices have shown promising properties such as high resistance to aqueous alteration and radiation damage.[2,26,29–32]

In rare-earth phosphates (REPO$_4$), the incorporation of tetravalent uranium and thorium into the structure occurs mainly through two different substitution mechanisms. The one most reported is the coupled cationic substitution:

$$2\ RE^{3+} \leftrightarrow Ca^{2+} + AN^{4+} \tag{1}$$

Such substitution was first reported in minerals by Förster[6] and then confirmed in different synthetic compounds.[25,33,34] The second mode of incorporation of tetravalent elements into the phosphate minerals is through the formation of solid solution between REPO$_4$ and ANSiO$_4$ compounds. This occurs through simultaneous substitution in the cationic and anionic sites:

$$RE^{3+} + PO_4^{3-} \leftrightarrow (Th,U)^{4+} + SiO_4^{4-} \tag{2}$$
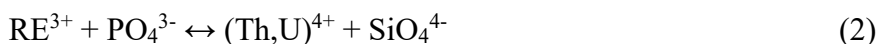
These substitutions were reported to exist in natural mineral phases.[35] One of the first examples of synthetic Th- and U-containing phosphosilicates was reported by McCarthy $et\ al.$[36] In that study, phase-pure RE$_{0.7}$Th$_{0.27}$U$_{0.03}$(PO$_4$)$_{0.7}$(SiO$_4$)$_{0.3}$ (RE = Gd, Nd, Ce, La, Pr, Sm, Y) samples were synthesized using a coprecipitation method. Mesbah $et\ al.$ synthesized Th$_x$Er$_{1-x}$(SiO$_4$)$_x$(PO$_4$)$_{1-x}$ samples in the entire compositional range by a hydrothermal method.[37] Thermodynamic behavior of this system was not assessed then, despite its importance to nuclear waste applications and hence, in this study we continue to investigate the Th$_x$Er$_{1-x}$(SiO$_4$)$_x$(PO$_4$)$_{1-x}$ solid solution from a thermochemical perspective. We also review the structural properties of this system after prolonged storage and heating.

2. MATERIALS AND METHODS

Synthesis

The Th$_x$Er$_{1-x}$(SiO$_4$)$_x$(PO$_4$)$_{1-x}$ solid solution series in the entire compositional range ($0 \leq x \leq 1$) were synthesized hydrothermally.[37] Th(NO$_3$)$_4$·4-5H$_2$O, ErCl$_3$·nH$_2$O, NaOH, NaHCO$_3$, Na$_2$SiO$_3$, H$_3$PO$_4$ (all analytical grade supplied by Sigma-Aldrich) were the reactants. For each composition, aqueous solutions containing Er and Th were added dropwise to an anionic solution containing precise amounts of Na$_2$SiO$_3$ and H$_3$PO$_4$. Then the pH of the solution was raised to 11.3 using NaOH (8M), and finally adjusted to 8.7 by NaHCO$_3$ buffer. The final mixture was transferred into a teflon-lined acid digestion bomb (Parr) and held for 7 days at 250 °C. The final product was washed twice with water and once with ethanol. The samples were thus stored in airtight containers for 2 years prior to thermodynamic analysis. Appropriate care was taken for handling thorium, which is a long-life α-emitter. The list of samples with their compositions measured by EDX is given in **Table 1**. One sample with composition Th$_{0.2}$Er$_{0.8}$(SiO$_4$)$_{0.2}$(PO$_4$)$_{0.8}$ was synthesized separately following the same procedure for the $in\ situ$ PXRD analysis, but the time before the experiment was less than a month.

Table 1. Composition of the Th$_x$Er$_{1-x}$(SiO$_4$)$_x$(PO$_4$)$_{1-x}$ samples as reported in [37].

Sample name[#]	x	Th	Er	Si	P	Actual composition of xenotime
10Th	0.1	0.11	0.89	0.14	0.86	Th$_{0.11}$Er$_{0.89}$(SiO$_4$)$_{0.11}$(PO$_4$)$_{0.89}$
20Th	0.2	0.19	0.81	0.26	0.74	Th$_{0.19}$Er$_{0.81}$(SiO$_4$)$_{0.19}$(PO$_4$)$_{0.81}$
30Th	0.3	0.25	0.75	0.30	0.70	Th$_{0.25}$Er$_{0.75}$(SiO$_4$)$_{0.25}$(PO$_4$)$_{0.75}$
40Th	0.4	0.43	0.57	0.47	0.53	Th$_{0.43}$Er$_{0.57}$(SiO$_4$)$_{0.43}$(PO$_4$)$_{0.57}$
50Th	0.5	0.44	0.56	0.55	0.45	Th$_{0.44}$Er$_{0.56}$(SiO$_4$)$_{0.44}$(PO$_4$)$_{0.56}$
60Th	0.6	0.56	0.44	0.65	0.35	Th$_{0.56}$Er$_{0.44}$(SiO$_4$)$_{0.56}$(PO$_4$)$_{0.44}$

70Th	0.7	0.64	0.36	0.73	0.27	$Th_{0.64}Er_{0.36}(SiO_4)_{0.64}(PO_4)_{0.36}$
80Th	0.8	0.76	0.24	0.84	0.16	$Th_{0.76}Er_{0.24}(SiO_4)_{0.76}(PO_4)_{0.24}$
90Th	0.9	0.88	0.12	0.95	0.05	$Th_{0.88}Er_{0.11}(SiO_4)_{0.88}(PO_4)_{0.11}$

[#]The numbers of "xTh" represent the approximate mole fraction of Th in the sample

Powder X-Ray Diffraction (PXRD)

Powder X-ray diffraction (PXRD) was performed on a Bruker AXS-D8 Advance diffractometer (Bruker-AXS, Inc., Billerica, MA) operated at 40 kV accelerating voltage with 40 mA emission current using a copper X-ray target for the initial phase check and to find lattice constants of the final samples. The data were collected from 20 to 80 °2θ using a step size of 0.012 °2θ. The PXRD patterns were further analyzed for the determination of lattice parameters by a whole profile fitting procedure (Jade v6.11, 2002, Materials Data Inc., Livermore, CA).

The *in situ* PXRD experiments were conducted on a separately synthesized $Th_{0.2}Er_{0.8}(SiO_4)_{0.2}(PO_4)_{0.8}$ using a Bruker Model D8 X-ray diffractometer equipped with a curved Ge-monochromator (111), a Cu X-ray source (40 kV,40 mA), a Lynx Eye position-sensitive detector, and Anton Paar HTK 2000 chamber. The data were collected from 2θ = 5 to 100° using a step size of 0.012° 2θ. Patterns were collected at 100 °C intervals to 1100 °C. They were further analyzed by the Rietveld method with General Structure Analysis System (GSAS) software version II.[38] The instrument parameters were obtained using a LaB_6 standard, the background was modelled with a Chebyshev function (8 terms), and the peak profiles were fitted with pseudo-Voigt convolution functions.[39] Detailed procedures to analyze the XRD data were described previously elsewhere.[40,41]

Calorimetry and Thermal Analysis

High temperature oxide melt solution calorimetry was performed using a custom-built Tian-Calvet twin calorimeter. Approximately 5 mg of sample was hand-pressed into a pellet to drop from room temperature into 20 g of molten lead borate ($2PbO \cdot B_2O_3$ at 800 °C). Oxygen was bubbled (5 mL/min) through the solvent and flushed (70 mL/min) through the gas space above it to enhance dissolution and maintain an oxidizing atmosphere. The heat effect was evaluated using Calisto software by integrating the thermopile signal over time. The methodology adopted in this study was identical to that in prior studies on similar systems.[31,42–44]

Simultaneous TGA-DSC analyses were performed with a Netzsch STA 449 C instrument coupled with a Micromeritics Cirrus 2 quadrupole mass spectrometer. The samples were annealed in a Pt pan in air from room temperature up to 1000 °C with a heating rate of 10 °C/min. The change in the mass of the sample was monitored and the gases evolved during the heating process were introduced into the ionization chamber of mass spectrometer. The signals were corrected by the reference baselines from runs with empty crucibles under the same experimental conditions. After TGA-DSC experiments, the samples were recovered for additional characterization.

Infrared Spectroscopy

Attenuated total reflectance-Fourier transform infrared (ATR-FTIR) spectra of all the samples were recorded using a Bruker Model Alpha-P IR spectrometer (diamond ATR cell, 4 cm^{-1} resolution, 400-4000 cm^{-1}).

3. RESULTS AND DISCUSSION

TGA-DSC-MS

TGA-DSC scans and corresponding MS signals for the samples 20Th and 80Th are shown in *Figure 1* (see *Figure 1S* in supplementary information for the rest of the scans). While MS was performed without any calibration and remained qualitative rather than quantitative, we could identify which gases evolved during heating.
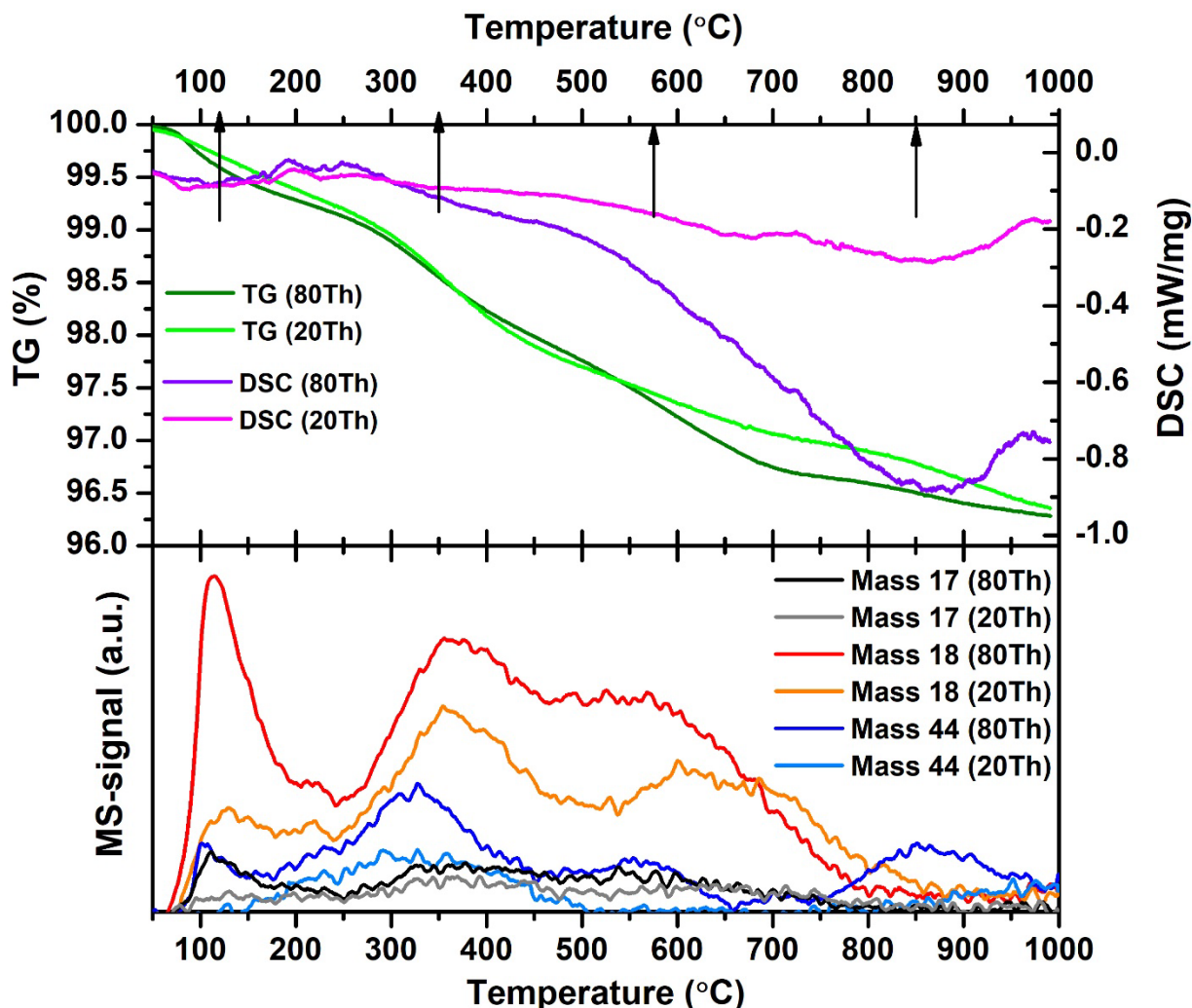

Figure 1. TGA-DSC scans with exothermic direction up (top) and MS signals (bottom) obtained for 20Th and 80Th samples. The arrows point to the temperatures of MS-peaks.

During annealing, the samples experienced a stepwise mass loss of 3-5 wt.% without any significant heat signal at low temperatures, which was surprising considering the coupled results from mass-spectrometry showing H_2O loss (signal from mass 18). Other possible species could be NH_3 (mass 17) and CO_2 (mass 44). Water loss is accompanied by heat uptake that is usually well defined in the DSC scans. The apparent weakness of this endotherm might be a result of possible exothermic processes (from crystallization of the secondary phases) occurring simultaneously. Another possible explanation could be the relatively small grain size of the samples that could also affect the desorption energetics and kinetics and move some of the water loss to the broad peaks at higher temperatures ($\sim$ 700 °C). A portion of water present in the samples is the consequence of high surface area leading to

significant surface adsorbed water where SEM of $Th_xEr_{1-x}(SiO_4)_x(PO_4)_{1-x}$ performed in another study [37] revealed the presence of nanometric sized needle-shaped grains (200 - 800 nm in length). The other portion of water which was only removed at higher temperature above 200 °C could be due to confinement inside the crystal structure (along the c-axis channel), which has been demonstrated in a previous structural study on $CeSiO_4$ and $USiO_4$, isostructural to $Th_xEr_{1-x}(SiO_4)_x(PO_4)_{1-x}$.[45] The calculated mole fraction of adsorbed water (assuming that the mass loss coming from other species is negligible) varies around 0.5 mole H_2O per mole of sample regardless of composition (see **Table 2**). The suggested presence of small amounts of ammonia and carbonaceous gases could be the result of the low temperature synthesis.

Powder X-Ray Diffraction

The structures of as prepared and post TGA-DSC (annealed at 1000 °C) samples were studied using PXRD. The PXRD patterns of the as-prepared and annealed samples are given in **Figure 2**.
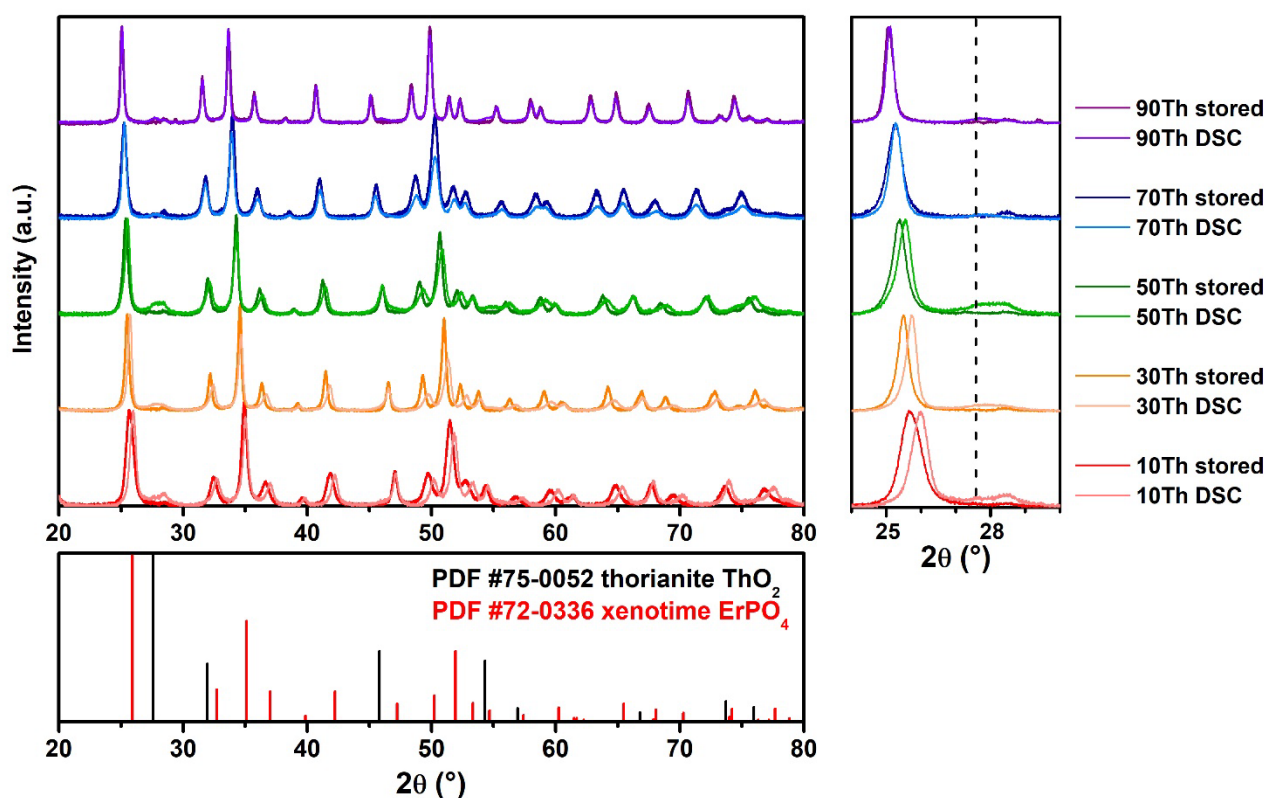
Figure 2. (Top) XRD scans of samples before (as prepared) and after heat treatment (DSC) with the insert of zoomed 24 - 30° 2θ region (dashed line represents reflections assigned to ThO_2). (Bottom) PDFs of the xenotime $ErPO_4$ and fluorite ThO_2 (thorianite), which is the impurity phase.

For the "stored" samples, the peaks exhibit broadening due to the nanosized character of the materials. In addition, extra reflections were noticeable. First, they could result from the formation of a secondary phase. The PXRD suggests it may be cubic thorianite, ThO_2. According to a recent study on thorium silicate ($ThSiO_4$),[46] thorianite was also observed, as a minor phase, during the synthesis of $ThSiO_4$ at lower pH. It must be noted that the thorianite phase was not present on the scans reported in the previous work by Mesbah *et al.*[37]. In the present study, the $Th_xEr_{1-x}(SiO_4)_x(PO_4)_{1-x}$ samples

were stored for two years prior to the TGA-DSC and high temperature solution calorimetry experiments. Consequently, ThO_2 might have been formed as poorly crystalline material, nevertheless noticeable on "stored" scans and then crystallized and/or coarsened after heating to 1000 °C on "DSC" scans. This is possible according to the equilibrium similar to other silicates.[44,47]

$$ThSiO_4 \rightleftarrows ThO_2 + SiO_2 \tag{3}$$

where thorianite is crystallized and silica remains amorphous that is not sensitive to XRD. The Rietveld refinement of the phase composition resulted in average of ~2-4 wt.% of ThO_2 and up to ~11 wt.% in some samples (see **Table 2**). The obtained values do not correlate with the overall Th-content in the samples from EDX and do not account for all the reflections seen in **Figure 2**. Although they could not be refined well, the unidentified reflections might be attributed to possible solid solution of Er_2O_3 in ThO_2 that would shift the peaks to higher angles. Solid solutions of thoria with rare earth elements are known and have been studied before.[48,49]

Another possible explanation of the emerging extra reflections at lower angles could come from the ordering of the defects. Although such effects were not discussed in these systems before, several studies discussed superstructure ordering on the anion sublattice (i.e. defect fluorite – pyrochlore – weberite[50,51] or fluorite – bixbyite[52]) and the cation sublattice (i.e. spinels[53]). In the Th-Er xenotime system, the incorporation of Er^{3+} into thorite structure would result in the formation of the oxygen vacancies for charge balance if there was not enough phosphorus in the system. If the sample composition was initially stoichiometric but had exsolved thoria as suggested by PXRD, the remaining xenotime would be Er-enriched, which could be consistent with such possible defect chemistry. Moreover, after the heat treatment, the positions of the main peaks moved to slightly higher angles (smaller lattice parameters). According to a previous study on $CeSiO_4$, isostructural to $Th_xEr_{1-x}(SiO_4)_x(PO_4)_{1-x}$, this was partially due to the removal of confined water that led to the contraction of unit cell volume.[45]

The changes in unit cell parameters and volume as a function of Th-content in the samples are reported in **Figure 3**. The unit cell parameters a and c both decreased linearly with that of the Th-content in both series of samples. However, the parameter a changed more steeply in the annealed samples. This resulted in decrease of the unit cell volume of the annealed samples compared to the stored samples. Moreover, this difference only affected samples with low Th-content, becoming almost negligible for Th-content > 0.6. Such behavior in the Th-poor end could reflect defect and PO_4^{3-} polyhedral ordering.
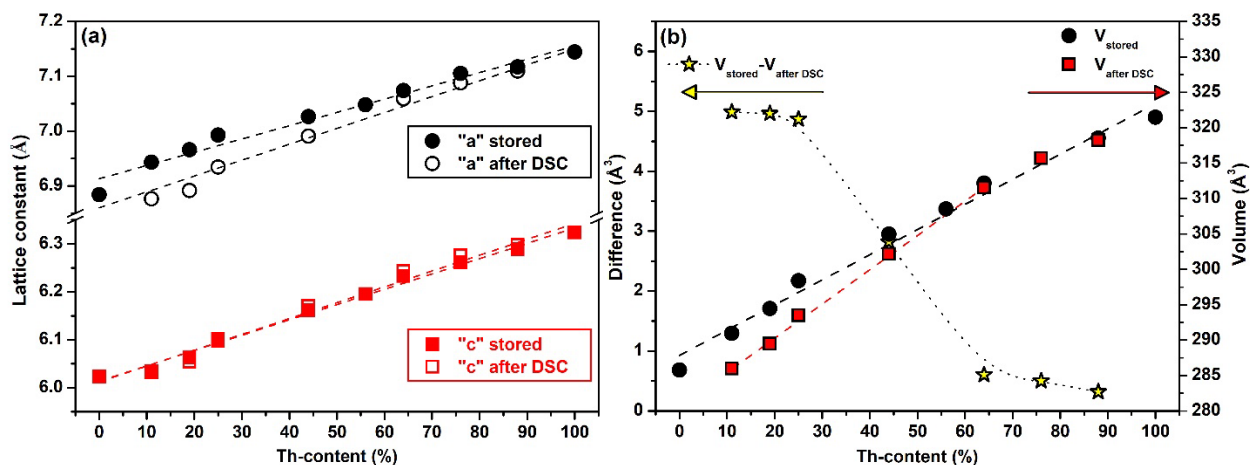
Figure 3. (a) Variation of the unit cell parameters *a* and *c* versus the thorium content in the prepared samples before (filled symbols) and after (open symbols) heat treatment at 1000 °C; (b) Variation of the unit cell volume versus the thorium content. The dotted curve was drawn to guide the eye while dashed lines correspond to linear fits of the obtained data. The error bars for this figure are within ± 0.0005 Å and overlap with the symbols, therefore we have omitted them.

Table 2. Extra components in the samples as estimated by TGA and XRD analysis.

| Sample name	Water content from TGA	ThO₂ content from XRD	
		Stored	**After heating in DSC**
10Th	0.787*	0.017	0.107
20Th	0.503	0.030	0.144
30Th	0.461	0.046	0.199
50Th	0.497	0.071	0.193
70Th	0.501	0.022	0.058
80Th	0.568	0.025	0.139
90Th	0.525	0.089	0.106

* This sample also exhibited large exothermic effect presumably coming from some organic impurities

In situ high temperature PXRD measurements were carried out on a separately synthesized $Th_{0.2}Er_{0.8}(SiO_4)_{0.2}(PO_4)_{0.8}$ sample to determine the structural stability as a function of temperature. (***Figure 4***). ***Figure 4*** shows that small shoulder peaks appeared around $2\theta = 27.7$ and 46° above 800 °C, indicating the formation of thorianite. This peak due to ThO_2 increased in intensity with increasing temperature and indicates the increase in the crystallinity of ThO_2, which was confirmed by Rietveld refinement of the sample heated at 1100 °C (***Figure 5*** and ***Figure 6***). At 1100 °C, a new set of diffraction peaks emerged (including the obvious peak at 30°), which could be due to the formation of huttonite, either from the transformation of decomposed thorite or the reaction of ThO_2 with SiO_2. This experiment also showed that there are no secondary phases in the "fresh" samples (as reported in [37]) compared to those studied after a prolonged storage time (***Figure 2***).
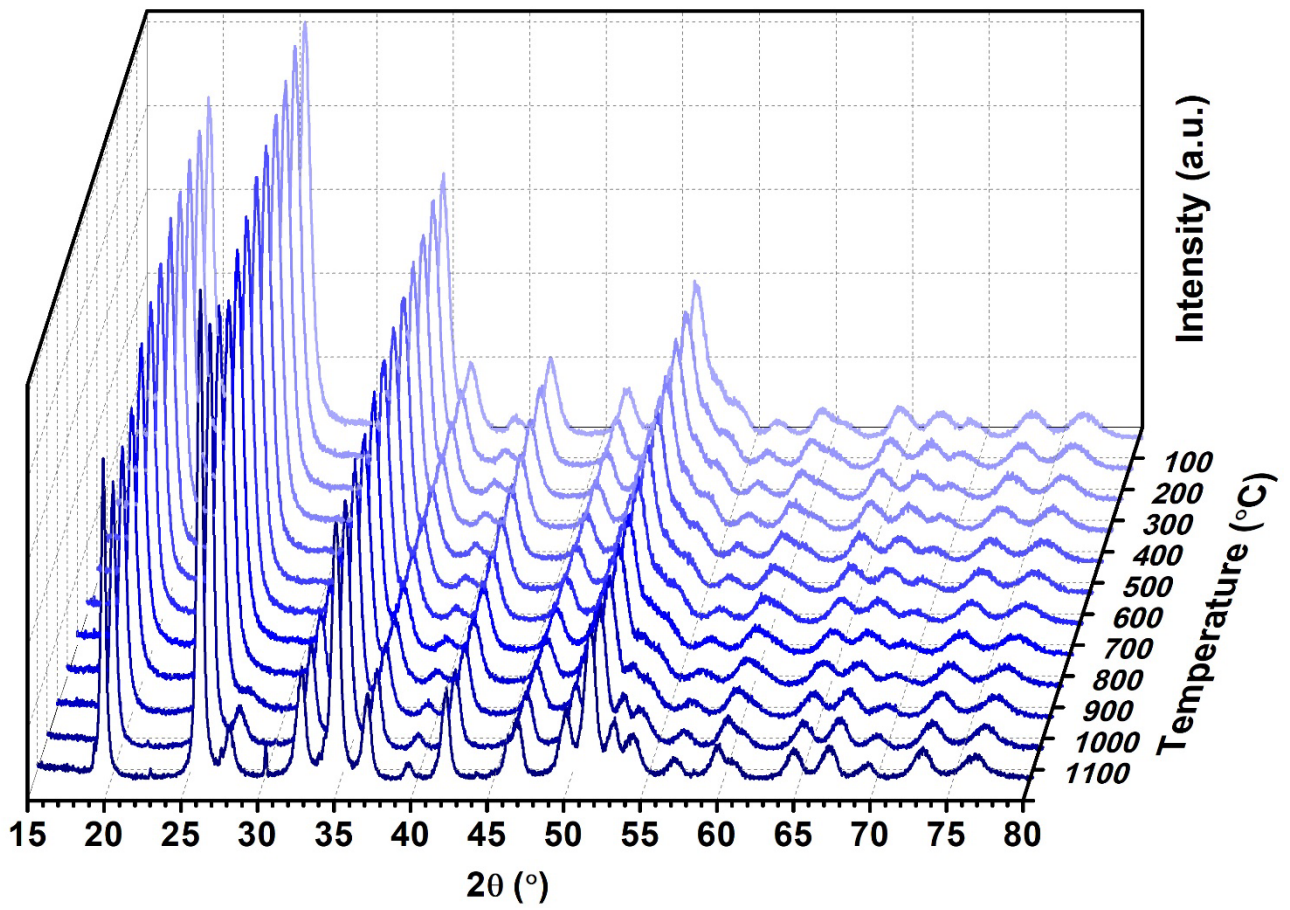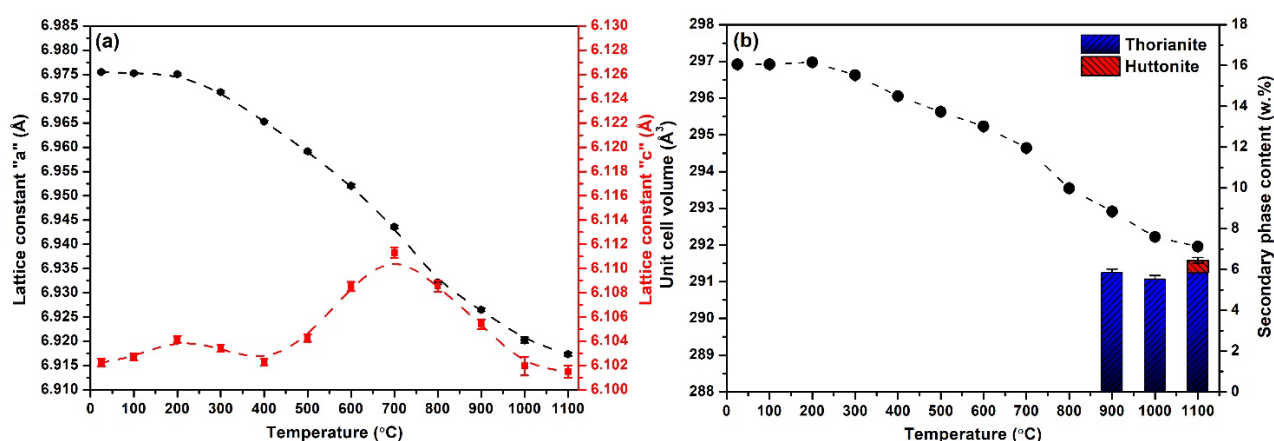
Figure 4. *In situ* PXRD patterns of $Th_{0.2}Er_{0.8}(SiO_4)_{0.2}(PO_4)_{0.8}$ from 25 to 1100 °C.
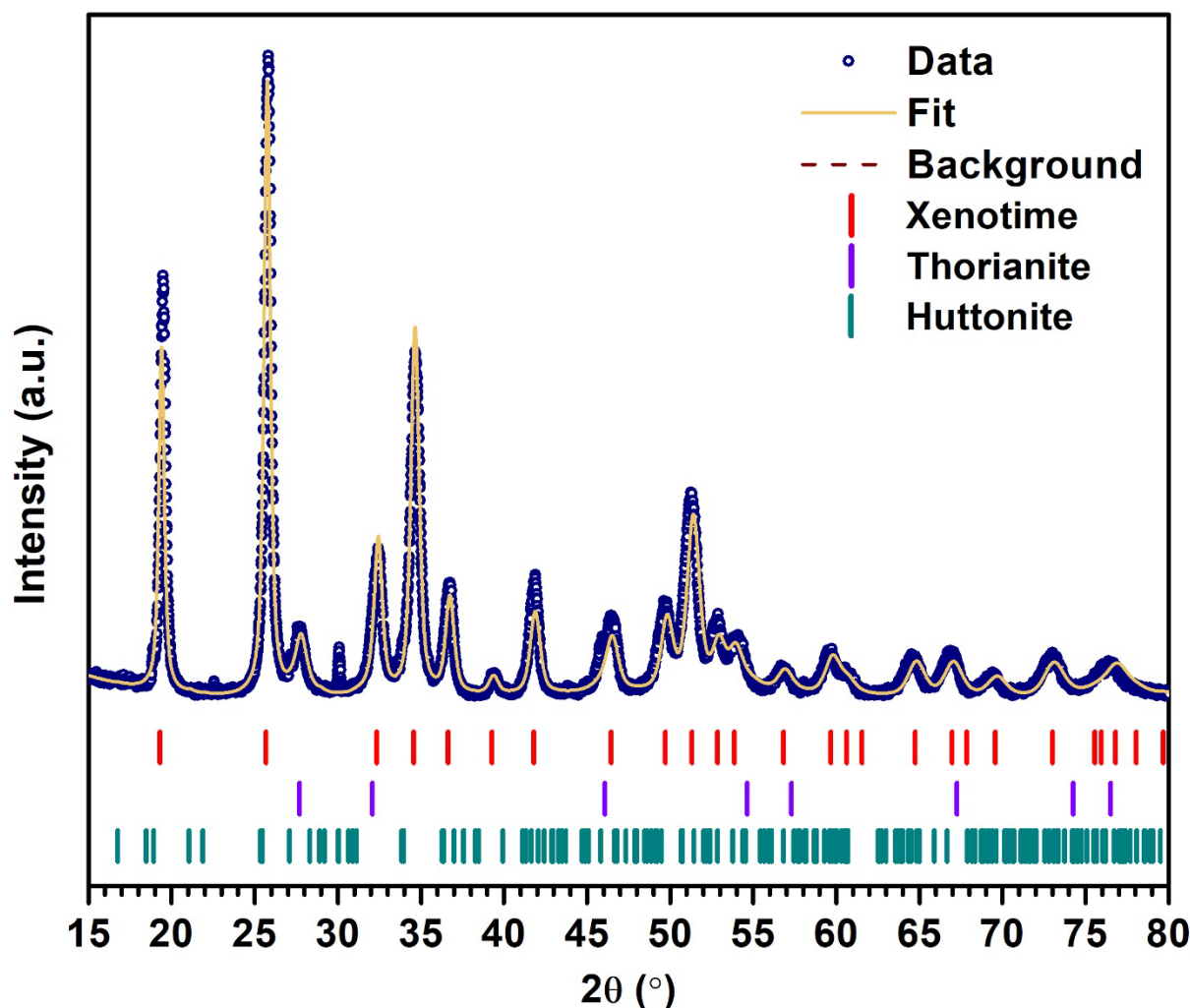
Figure 5. Fitted PXRD pattern of $Th_{0.2}Er_{0.8}(SiO_4)_{0.2}(PO_4)_{0.8}$ at 1100 °C. Data are shown as open blue circles. The fitting excludes the minor huttonite phase, which was poorly crystalized.

Figure 6. (a) Variation of unit cell parameters for $Th_{0.2}Er_{0.8}(SiO_4)_{0.2}(PO_4)_{0.8}$; and (b) Variation of unit cell volume and content of secondary phases (ThO_2 and huttonite), as the function of temperature.

Increase in temperature reveals nonlinear and anisotropic behavior of the unit cell parameters (***Figure 6***). The unit cell parameter *a* remained almost unchanged until 200 °C, then decreased, while the parameter *c* expanded until 700 °C, then decreased at high temperatures. Similar nonlinear thermal

behavior was reported for $CeSiO_4$ by Strzelecki *et al*,[45] which has a lattice contraction in the *a-(b-)* axis that was attributed to the removal of confined water from the [001] channels. This finding also agrees with the TG-DSC-MS data (***Figure 1***) where the evolution of several gases is reported. This leads to lattice parameter "c" expansion and contraction. The overall contraction of the unit cell is possibly a consequence of material sintering upon heating. Similar to this work, previous studies also reported the decomposition of xenotime (zircon) phase into a fluorite phase.[45,54]

Infrared Spectra

Solid-state ATR-FTIR spectra before and after DSC for the sample 30Th are presented in ***Figure 7***.
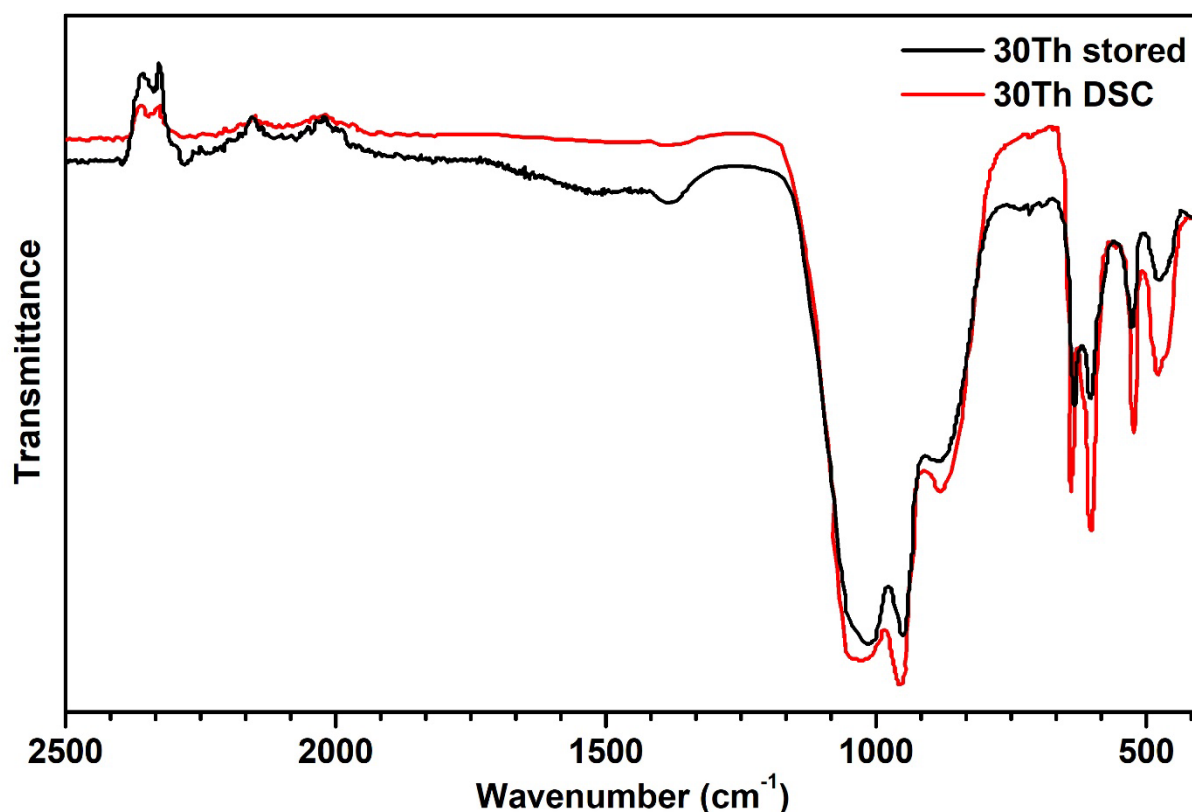
Figure 7.   Solid-state ATR-FTIR spectra of sample $Th_{0.3}Er_{0.7}(SiO_4)_{0.3}(PO_4)_{0.7}$ before and after DSC.

The bands associated with water (1400 – 2100 cm^{-1}) and carbonate (2200 – 2400 cm^{-1}) are smaller after the heat treatment, consistent with degassing upon heating. The PO_4^{3-} and SiO_4^{4-} bands (700-1200 cm^{-1}) are larger and some of their features (850 cm^{-1} and 1050 cm^{-1}) are sharper. This may imply that local ordering of PO_4^{3-} and SiO_4^{4-} polyhedra increases after heat treatment. It was shown in the previous study that the shape of these features changes with increase in Th-content [37].

High Temperature Oxide Melt Solution Calorimetry

The enthalpies of drop solution (ΔH_{ds}) of the stored and annealed samples are given in ***Table 3***. As these samples contain both adsorbed water and some oxide impurities, their amounts have been accounted for in the thermochemical cycle (see ***Table 4*** for the details of correction). The corrected

values are also given in *Table 3* along with the calculated values of the enthalpies of mixing (ΔH_{mix}) and formation from oxides ($\Delta H_{\text{f,ox}}$). The measured values are plotted in *Figure 8* along with those of the stable zircon-type structure end members, xenotime ErPO$_4$ and thorite ThSiO$_4$.

Table 3. Solution calorimetric data for the samples before and after DSC: enthalpy of drop solution as measured (ΔH_{ds}), enthalpy of drop solution corrected for water (ΔH^*_{ds}(stored)), enthalpy of drop solution corrected for the presence of ThO$_2$ (ΔH^*_{ds}(DSC)), enthalpy of mixing (ΔH_{mix}) and enthalpy of formation from oxides ($\Delta H_{\text{f,ox}}$).

| Sample name	Before DSC				After DSC			
	ΔH_{ds}(stored) kJ/mol	ΔH^*_{ds}(stored) kJ/mol	ΔH_{mix}(stored) kJ/mol	$\Delta H_{\text{f,ox}}$(stored) kJ/mol	ΔH_{ds}(DSC) kJ/mol	ΔH^*_{ds}(DSC) kJ/mol	ΔH_{mix}(DSC) kJ/mol	$\Delta H_{\text{f,ox}}$(DSC) kJ/mol
ErPO$_4$	129.85$	-	-	-275.6 ± 1.9[55]	129.85	129.85	0	-275.6 ± 1.9
Th10	160.10 ± 1.65(7)	117.60 ± 1.65	15.0 ± 2.4	-231.0 ± 5.6	142.21 ± 1.18(2)	131.72 ± 1.18	0.8 ± 2.1	-245.2 ± 5.4
Th20	186.28 ± 0.42(6)	140.50 ± 0.42	-6.0 ± 2.4	-230.4 ± 5.1	151.12 ± 2.32(2)	136.98 ± 2.32	-2.5 ± 3.3	-226.9 ± 5.6
Th30	172.26 ± 1.98(6)	132.14 ± 1.98	3.9 ± 3.3	-204.5 ± 5.3	150.06 ± 1.70(2)	130.55 ± 1.70	5.4 ± 3.2	-202.9 ± 5.2
Th50	176.79 ± 1.12(6)	129.91 ± 1.12	10.7 ± 3.8	-146.4 ± 4.5	154.91 ± 2.01(2)	135.93 ± 2.01	4.7 ± 4.1	-152.4 ± 4.8
Th70	181.64 ± 0.66(6)	141.88 ± 0.66	3.7 ± 4.4	-99.6 ± 3.7	150.17 ± 0.99(2)	144.52 ± 0.99	1.0 ± 4.4	-102.3 ± 3.8
Th80	202.18 ± 0.40(5)	154.38 ± 0.40	-1.8 ± 4.7	-72.8 ± 3.2	179.22 ± 2.41(3)	165.60 ± 2.41	-17.1 ± 5.3	-88.1 ± 4.0
Th90	204.08 ± 1.55(6)[#]	154.40 ± 1.55	-2.9 ± 5.3	-41.6 ± 3.0	174.14 ± 1.96(3)	163.77 ± 1.96	-12.3 ± 5.4	-51.0 ± 3.2
ThSiO$_4$	154.40 ± 5.4[54]	-	-	-6.4 ± 5.7[54]	154.40 ± 5.40	-	0	-6.4 ± 5.7

[*]values, corrected for water (as is) and ThO$_2$ (after DSC) content
[#]this value might not reflect the general trend due to the presence of possible impurities
[$]This value is synthetic as it was back-calculated from the enthalpy of formation (-275.6 ± 1.9 kJ/mol [55])

The remaining small differences, after correction for water and impurity phases, obtained between stored and annealed samples could arise from a combination of other effects, such as the slight grain growth and/or ordering of defects either from charge balance or exsolution of ThO$_2$. However, the overall heat effect of dissolution was not strongly affected by heating to 1000 °C in DSC and the values for annealed and stored samples lie within likely experimental error, especially when one considers possible changes in composition and exsolution in addition to the statistical error of the calorimetric measurements. Despite these small differences, we can state that the thorite-xenotime solid solution was stable with respect to binary oxides but showed a complex (nominally subregular) enthalpy of mixing.
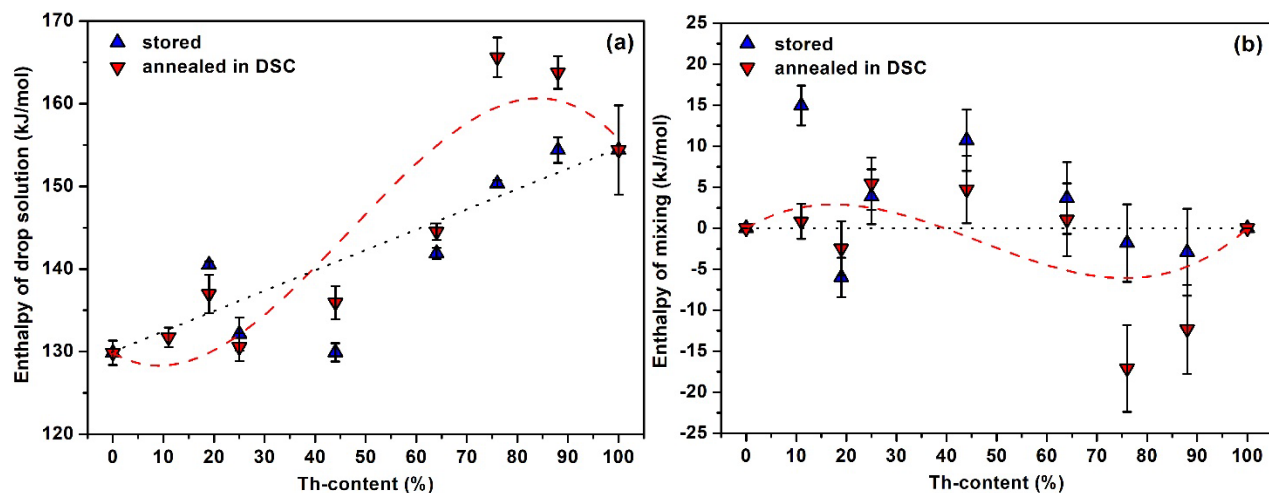
Figure 8. (a) Enthalpy of drop solution of stored samples and samples after DSC. (b) Enthalpy of mixing of the stored samples and samples after DSC. Dashed curves represent polynomial fits using the whole set of data. Dotted lines represent zero heat of mixing.

Fitting both series of data together requires the subregular solution model. Heats of mixing are slightly endothermic on the thorium-depleted side and slightly exothermic on the thorium-enriched side. The interaction is not large. Indeed, mixing enthalpies are mainly less than 15 kJ/mol in magnitude. Thus, there is a little driving force for exsolution or ternary phase formation and the solid solutions can be viewed as continuous at all accessible temperatures. Margules parameters can be estimated from the fitted polynomial function:

$$\Delta H_{mix} = W(x) \cdot x \cdot (1-x) = (W_1 \cdot (1-x) + W_2 \cdot x) \cdot x \cdot (1-x), \tag{4}$$

from which $W_1 = 73.1 \pm 20.1$ kJ/mol and $W_2 = -52.6 \pm 45.6$ kJ/mol and the overall Margules function is:

$$W(x) = (73.1 \pm 20.1) - (125.7 \pm 49.8) \cdot x \tag{5}$$

This complex energetic behavior may reflect the simultaneous substitution of silicon and phosphorus and of thorium and erbium on different sites in the crystal structure and possible short-range order as observed previously by Mesbah *et al.*[37] Indeed, it has been shown that the Th-O distances do not evolve in the same way as the Er-O distances in the thorite-xenotime solid solution.

Table 4. Thermochemical cycle used to calculate water correction for the enthalpies of drop solution and for the calculation of the enthalpy of formation from oxides.

Reaction	Enthalpy, kJ/mol
$(ThSiO_4)_x(ErPO_4)_{1-x\,(s,25)} \rightarrow$ $\rightarrow x(ThO_{2(sln,800)} + SiO_{2(sln,800)}) + \dfrac{(1-x)}{2}(Er_2O_{3(sln,800)} + P_2O_{5(sln,800)})$	ΔH_{ds} (see **Table 3**)
$ThO_{2(s,25)} \rightarrow ThO_{2(sln,800)}$	$\Delta H_{ds}(ThO_2) = 98.1 \pm 1.7^{56}$
$SiO_{2(s,25)} \rightarrow SiO_{2(sln,800)}$	$\Delta H_{ds}(SiO_2) = 47.9 \pm 0.6^{57}$
$Er_2O_{3(s,25)} \rightarrow Er_2O_{3(sln,800)}$	$\Delta H_{ds}(Er_2O_3) = 50.6 \pm 0.4^{58}$
$P_2O_{5(s,25)} \rightarrow P_2O_{5(sln,800)}$	$\Delta H_{ds}(P_2O_5) = -342.1 \pm 7.9^{59}$
$H_2O_{(l,25)} \rightarrow H_2O_{(g,800)}$	$\Delta H_{heat} = 73.2^{60}$
$x(ThO_{2(s,25)} + SiO_{2(s,25)}) + \dfrac{(1-x)}{2}(Er_2O_{3(s,25)} + P_2O_{5(s,25)}) \rightarrow (ThSiO_4)_x(ErPO_4)_{1-x\,(s,25)}$	$\Delta H_{f,ox}$ (see **Table 3**)

Correction for water:
$$\Delta H^*_{ds} = \Delta H_{ds} - n \times \Delta H_{heat}$$

Enthalpy of formation from oxides:
$$\Delta H_{f,ox} = -\Delta H^*_{ds} + x \times [\Delta H_{ds}(ThO_2) + \Delta H_{ds}(SiO_2)] + \dfrac{(1-x)}{2} \times [\Delta H_{ds}(Er_2O_3) + \Delta H_{ds}(P_2O_5)]$$

Enthalpy of mixing:
$$\Delta H_{mix} = -\Delta H^*_{ds} + x \times \Delta H_{ds}(ThSiO_4, thorite) + (1-x)\Delta H_{ds}(ErPO_4)$$

Enthalpy of formation from oxides was also calculated through a thermodynamic cycle and the resulting values are given in **Table 3** and plotted in **Figure 9**.
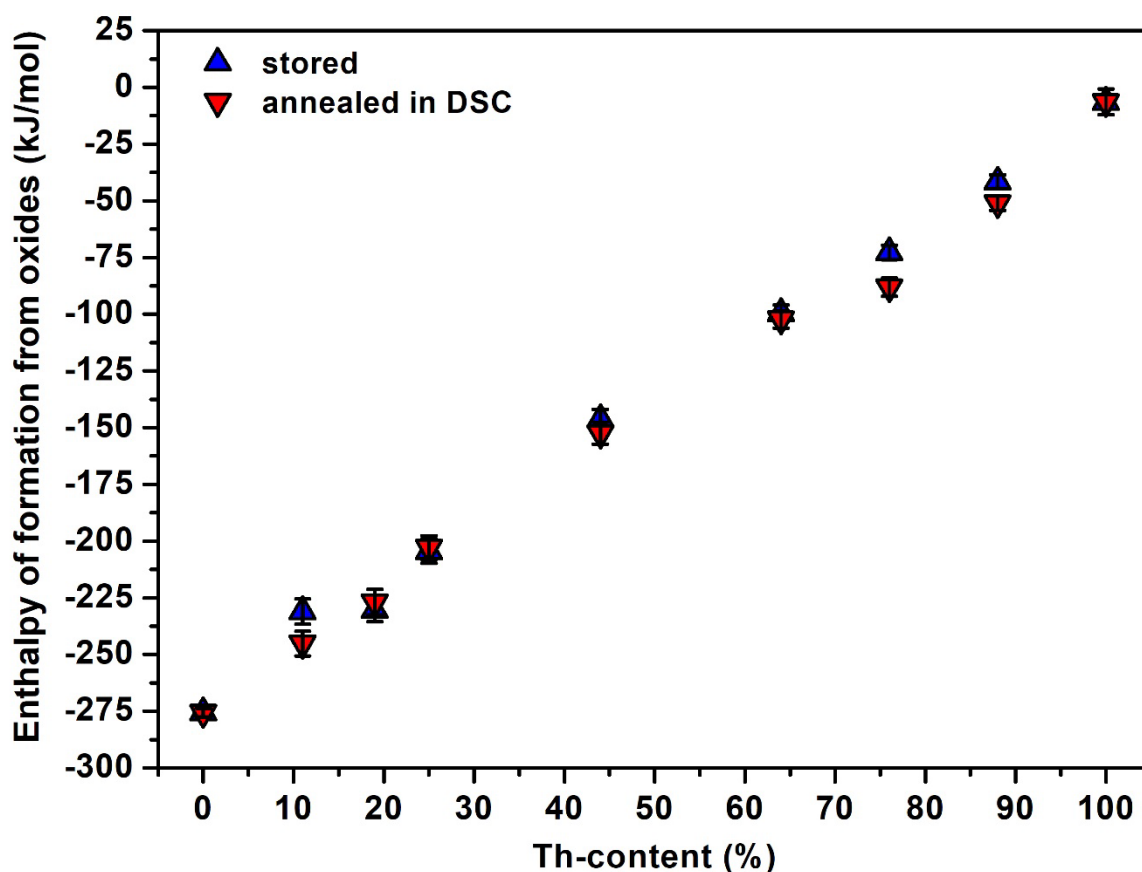
Figure 9. Enthalpy of formation from oxides before and after DSC.

The approximately linear trend in **Figure 9** indicates that the small mixing enthalpies are masked by the large approximately linear destabilization with increasing Th-content. This destabilization reflects the greater stability or the phosphate endmember compared to the silicate.

4. CONCLUSION

The non-linear unit cell volume expansion is a feature of the zircon-type structure shown for several similar systems. It is also common that upon heating, such materials mainly maintain the $I4_1/amd$ symmetry, but after 700 °C, the fluorite phase can evolve. The ThSiO$_4$-ErPO$_4$ system forms a complete solid solution with small, but complex deviations from ideal mixing. This solid solution is predicted to be thermodynamically stable with respect to binary oxides with little driving force for either exsolution or intermediate compound formation, which is essential for a ceramic nuclear waste form. ErPO$_4$ is energetically more stable relative to oxide endmembers than ThSiO$_4$ substantially, resulting in an almost linear trend in enthalpy of formation versus thorianite content.

SUPPORTING INFORMATION

TGA-DSC scans of the samples studied in this work.

REFERENCES

(1) Boatner, L. A. Synthesis, Structure, and Properties of Monazite, Pretulite, and Xenotime. *Rev. Mineral. Geochemistry* **2002**, *48* (1), 87–121. https://doi.org/10.2138/rmg.2002.48.4.

(2) Rapp, R. P.; Watson, E. B. Monazite Solubility and Dissolution Kinetics: Implications for the Thorium and Light Rare Earth Chemistry of Felsic Magmas. *Contrib. to Mineral. Petrol.* **1986**, *94* (3), 304–316. https://doi.org/10.1007/BF00371439.

(3) Bowring, S.; Housh, T. The Earth's Early Evolution. *Science (80-.).* **1995**, *269* (5230), 1535–1540. https://doi.org/10.1126/science.7667634.

(4) Förster, H.-J. Composition and Origin of Intermediate Solid Solutions in the System Thorite-Xenotime-Zircon-Coffinite. *Lithos* **2006**, *88* (1–4), 35–55. https://doi.org/10.1016/j.lithos.2005.08.003.

(5) Ni, Y.; Hughes, J. M.; Mariano, A. N. Crystal Chemistry of the Monazite and Xenotime Structures. *Am. Mineral.* **1995**, *80* (1–2), 21–26. https://doi.org/10.2138/am-1995-1-203.

(6) Förster, H.-J. The Chemical Composition of REE-Y-Th-U-Rich Accessory Minerals in Peraluminous Granites of the Erzgebirge-Fichtelgebirge Region, Germany; Part I, The Monazite-(Ce)-Brabantite Solid Solution Series. *Am. Mineral.* **1998**, *83* (3–4), 259–272. https://doi.org/10.2138/am-1998-3-409.

(7) Bea, F. Residence of REE, Y, Th and U in Granites and Crustal Protoliths; Implications for the Chemistry of Crustal Melts. *J. Petrol.* **1996**, *37* (3), 521–552. https://doi.org/10.1093/petrology/37.3.521.

(8) Franz, G.; Andrehs, G.; Rhede, D. Crystal Chemistry of Monazite and Xenotime from Saxothuringian-Moldanubian Metapelites, NE Bavaria, Germany. *Eur. J. Mineral.* **1996**, *8* (5), 1097–1118. https://doi.org/10.1127/ejm/8/5/1097.

(9) Heinrich, W.; Rehs, G.; Franz, G. Monazite-Xenotime Miscibility Gap Thermometry. I. An Empirical Calibration. *J. Metamorph. Geol.* **1997**, *15* (1), 3–16. https://doi.org/10.1111/j.1525-1314.1997.t01-1-00052.x.

(10) Buick, R.; Brauhart, C. W. W.; Morant, P.; Thornett, J. R. R.; Maniw, J. G. G.; Archibald, N. J. J.; Doepel, M. G. G.; Fletcher, I. R. R.; Pickard, A. L. L.; Smith, J. B. B.; Barley, M. E. E.; McNaughton, N. J. J.; Groves, D. I. I. Geochronology and Stratigraphic Relationships of the Sulphur Springs Group and Strelley Granite: A Temporally Distinct Igneous Province in the Archaean Pilbara Craton, Australia. *Precambrian Res.* **2002**, *114* (1–2), 87–120. https://doi.org/10.1016/S0301-9268(01)00221-2.

(11) Buick, R.; Thornett, J. R.; McNaughton, N. J.; Smith, J. B.; Barley, M. E.; Savage, M. Record of Emergent Continental Crust ~3.5 Billion Years Ago in the Pilbara Craton of Australia. *Nature* **1995**, *375* (6532), 574–577. https://doi.org/10.1038/375574a0.

(12) Schärer, U.; Xu, R.-H. H.; Allègre, C. J. U-Pb Geochronology of Gangdese (Transhimalaya) Plutonism in the Lhasa-Xigaze Region, Tibet. *Earth Planet. Sci. Lett.* **1984**, *69* (2), 311–320. https://doi.org/10.1016/0012-821X(84)90190-0.

(13) Schärer, U. The Effect of Initial ^{230}Th Disequilibrium on Young U-Pb Ages: The Makalu Case, Himalaya. *Earth Planet. Sci. Lett.* **1984**, *67* (2), 191–204. https://doi.org/10.1016/0012-821X(84)90114-6.

(14) Bowring, S. A.; Erwin, D. H. H.; Jin, Y. G. G.; Martin, M. W. W.; Davidek, K.; Wang, W. U/Pb Zircon Geochronology and Tempo of the End-Permian Mass Extinction. *Science (80-.).* **1998**, *280* (5366), 1039–1045. https://doi.org/10.1126/science.280.5366.1039.

(15) Gibson, G. M.; Ireland, T. R. Granulite Formation during Continental Extension in Fiordland, New Zealand. *Nature* **1995**, *375* (6531), 479–482. https://doi.org/10.1038/375479a0.

(16) Seydoux-Guillaume, A.-M.; Wirth, R.; Heinrich, W.; Montel, J.-M. Experimental Determination of Thorium Partitioning between Monazite and Xenotime Using Analytical Electron Microscopy and X-

Ray Diffraction Rietveld Analysis. *Eur. J. Mineral.* **2002**, *14* (5), 869–878. https://doi.org/10.1127/0935-1221/2002/0014-0869.

(17) Rasmussen, B.; Fletcher, I. R.; Muhling, J. R.; Wilde, S. A. In Situ U-Th-Pb Geochronology of Monazite and Xenotime from the Jack Hills Belt: Implications for the Age of Deposition and Metamorphism of Hadean Zircons. *Precambrian Res.* **2010**, *180* (1–2), 26–46. https://doi.org/10.1016/j.precamres.2010.03.004.

(18) Rasmussen, B.; Fletcher, I. R.; Muhling, J. R. In Situ U-Pb Dating and Element Mapping of Three Generations of Monazite: Unravelling Cryptic Tectonothermal Events in Low-Grade Terranes. *Geochim. Cosmochim. Acta* **2007**, *71* (3), 670–690. https://doi.org/10.1016/j.gca.2006.10.020.

(19) Montel; Kornprobst; Vielzeuf. Preservation of Old U-Th-Pb Ages in Shielded Monazite: Example from the Beni Bousera Hercynian Kinzigites (Morocco). *J. Metamorph. Geol.* **2001**, *18* (3), 335-342. https://doi.org/10.1046/j.1525-1314.2000.00261.x.

(20) Montel, J.-M.; Razafimahatratra, D.; Ralison, B.; De Parseval, P.; Thibault, M.; Randranja, R. Monazite from Mountain to Ocean: A Case Study from Trolognaro (Fort-Dauphin), Madagascar. *Eur. J. Mineral.* **2011**, *23* (5), 745–757. https://doi.org/10.1127/0935-1221/2011/0023-2149.

(21) Dacheux, N.; Clavier, N.; Podor, R. Versatile Monazite: Resolving Geological Records and Solving Challenges in Materials Science: Monazite as a Promising Long-Term Radioactive Waste Matrix: Benefits of High-Structural Flexibility and Chemical Durability. *Am. Mineral.* **2013**, *98* (5–6), 833–847. https://doi.org/10.2138/am.2013.4307.

(22) Schlenz, H.; Heuser, J.; Neumann, A.; Schmitz, S.; Bosbach, D. Monazite as a Suitable Actinide Waste Form. *Zeitschrift für Krist. - Cryst. Mater.* **2013**, *228* (3), 113–123. https://doi.org/10.1524/zkri.2013.1597.

(23) Terra, O.; Dacheux, N.; Audubert, F.; Podor, R. Immobilization of Tetravalent Actinides in Phosphate Ceramics. *J. Nucl. Mater.* **2006**, *352* (1–3), 224–232. https://doi.org/10.1016/j.jnucmat.2006.02.058.

(24) Bregiroux, D.; Terra, O.; Audubert, F.; Dacheux, N.; Serin, V.; Podor, R.; Bernache-Assollant, D. Solid-State Synthesis of Monazite-Type Compounds Containing Tetravalent Elements. *Inorg. Chem.* **2007**, *46* (24), 10372–10382. https://doi.org/10.1021/ic7012123.

(25) Terra, O.; Dacheux, N.; Clavier, N.; Podor, R.; Audubert, F. Preparation of Optimized Uranium and Thorium Bearing Brabantite or Monazite/Brabantite Solid Solutions. *J. Am. Ceram. Soc.* **2008**, *91* (11), 3673–3682. https://doi.org/10.1111/j.1551-2916.2008.02678.x.

(26) Oelkers, E. H.; Montel, J.-M. Phosphates and Nuclear Waste Storage. *Elements* **2008**, *4* (2), 113–116. https://doi.org/10.2113/GSELEMENTS.4.2.113.

(27) Burakov, B. E.; Yagovkina, M. A.; Garbuzov, V. M.; Kitsay, A. A.; Zirlin, V. A. Self-Irradiation of Monazite Ceramics: Contrasting Behavior of $PuPO_4$ and $(La,Pu)PO_4$ Doped with Pu-238. *MRS Proc.* **2004**, *824*, CC4.1. https://doi.org/10.1557/PROC-824-CC4.1.

(28) Ewing, R. C.; Lutze, W.; Weber, W. J. Zircon: A Host-Phase for the Disposal of Weapons Plutonium. *J. Mater. Res.* **1995**, *10* (2), 243–246. https://doi.org/10.1557/JMR.1995.0243.

(29) Ewing, R. C.; Wang, L. Phosphates as Nuclear Waste Forms. *Rev. Mineral. Geochemistry* **2002**, *48* (1), 673–699. https://doi.org/10.2138/rmg.2002.48.18.

(30) Meldrum, A.; Boatner, L. A.; Ewing, R. C. A Comparison of Radiation Effects in Crystalline ABO_4-Type Phosphates and Silicates. *Mineral. Mag.* **2000**, *64* (2), 185–194. https://doi.org/10.1180/002646100549283.

(31) Shelyug, A.; Mesbah, A.; Szenknect, S.; Clavier, N.; Dacheux, N.; Navrotsky, A. Thermodynamics and Stability of Rhabdophanes, Hydrated Rare Earth Phosphates $REPO_4 \cdot nH_2O$. *Front. Chem.* **2018**, *6* (DEC). https://doi.org/10.3389/fchem.2018.00604.

(32) Rafiuddin, M. R.; Seydoux-Guillaume, A.-M.; Deschanels, X.; Mesbah, A.; Baumier, C.; Szenknect, S.; Dacheux, N. An In-Situ Electron Microscopy Study of Dual Ion-Beam Irradiated Xenotime-Type $ErPO_4$. *J. Nucl. Mater.* **2020**, *539*, 152265. https://doi.org/10.1016/j.jnucmat.2020.152265.

(33) Podor, R.; Cuney, M.; Nguyen, T. C. Experimental Study of the Solid Solution between Monazite-(La) and $(Ca_{0.5}U_{0.5})PO_4$ at 780 Degrees C and 200 MPa. *Am. Mineral.* **1995**, *80* (11–12), 1261–1268. https://doi.org/10.2138/am-1995-11-1215.

(34) Qin, D.; Mesbah, A.; Lautru, J.; Szenknect, S.; Dacheux, N.; Clavier, N. Reaction Sintering of Rhabdophane into Monazite-Cheralite $Nd_{1-2x}Th_xCa_xPO_4$ (x = 0-0.1) Ceramics. *J. Eur. Ceram. Soc.* **2020**, *40* (3), 911–922. https://doi.org/10.1016/j.jeurceramsoc.2019.10.050.

(35) Förster, H.-J.; Harlov, D. E. Monazite-(Ce)-Huttonite Solid Solutions in Granulite-Facies Metabasites from the Ivrea-Verbano Zone, Italy. *Mineral. Mag.* **1999**, *63* (4), 587–594.

https://doi.org/10.1180/002646199548637.

(36) McCarthy, G. J.; White, W. B.; Pfoertsch, D. E. Synthesis of Nuclear Waste Monazites, Ideal Actinide Hosts for Geologic Disposal. *Mater. Res. Bull.* **1978**, *13* (11), 1239–1245. https://doi.org/10.1016/0025-5408(78)90215-5.

(37) Mesbah, A.; Clavier, N.; Lozano-Rodriguez, M. J.; Szenknect, S.; Dacheux, N. Incorporation of Thorium in the Zircon Structure Type through the $Th_{1-x}Er_x(SiO_4)_{1-x}(PO_4)_x$ Thorite-Xenotime Solid Solution. *Inorg. Chem.* **2016**, *55* (21), 11273–11282. https://doi.org/10.1021/acs.inorgchem.6b01862.

(38) Toby, B. H.; Von Dreele, R. B. GSAS-II : The Genesis of a Modern Open-Source All Purpose Crystallography Software Package. *J. Appl. Crystallogr.* **2013**, *46* (2), 544–549. https://doi.org/10.1107/S0021889813003531.

(39) Thompson, P.; Cox, D. E.; Hastings, J. B. Rietveld Refinement of Debye-Scherrer Synchrotron x-Ray Data from Al_2O_3. *J. Appl. Crystallogr.* **1987**, *20* (2), 79–83. https://doi.org/10.1107/S0021889887087090.

(40) Guo, X.; Lü, X.; White, J. T.; Benmore, C. J.; Nelson, A. T.; Roback, R. C.; Xu, H. Bulk Moduli and High Pressure Crystal Structure of U_3Si_2. *J. Nucl. Mater.* **2019**, *523*, 135–142. https://doi.org/10.1016/j.jnucmat.2019.06.006.

(41) Strzelecki, A. C.; Kriegsman, K.; Estevenon, P.; Goncharov, V.; Bai, J.; Szenknect, S.; Mesbah, A.; Wu, D.; McCloy, J. S.; Dacheux, N.; Guo, X. High-Temperature Thermodynamics of Cerium Silicates, $A-Ce_2Si_2O_7$, and $Ce_{4.67}(SiO_4)_3O$. *ACS Earth Sp. Chem.* **2020**, *4* (11), 2129–2143. https://doi.org/10.1021/acsearthspacechem.0c00231.

(42) Neumeier, S.; Kegler, P.; Arinicheva, Y.; Shelyug, A.; Kowalski, P. M.; Schreinemachers, C.; Navrotsky, A.; Bosbach, D. Thermochemistry of $La_{1-x}Ln_xPO_4$ Monazites (Ln = Gd, Eu). *J. Chem. Thermodyn.* **2017**, *105*, 396–403. https://doi.org/10.1016/j.jct.2016.11.003.

(43) Zhang, L.; Shelyug, A.; Navrotsky, A. Thermochemistry of UO_2-ThO_2 and UO_2-ZrO_2 Fluorite Solid Solutions. *J. Chem. Thermodyn.* **2017**, *114*, 48–54. https://doi.org/10.1016/j.jct.2017.05.026.

(44) Strzelecki, A. C.; Bourgeois, C.; Kriegsman, K. W.; Estevenon, P.; Wei, N.; Szenknect, S.; Mesbah, A.; Wu, D.; Ewing, R. C.; Dacheux, N.; Guo, X. Thermodynamics of $CeSiO_4$: Implications for Actinide Orthosilicates. *Inorg. Chem.* **2020**, *59* (18), 13174–13183. https://doi.org/10.1021/acs.inorgchem.0c01476.

(45) Strzelecki, A. C.; Barral, T.; Estevenon, P.; Mesbah, A.; Goncharov, V.; Baker, J.; Bai, J.; Clavier, N.; Szenknect, S.; Migdisov, A.; Xu, H.; Ewing, R. C.; Dacheux, N.; Guo, X. The Role of Water and Hydroxyl Groups in the Structures of Stetindite and Coffinite, $MSiO_4$ (M = Ce, U). *Inorg. Chem.* **2021**, *4*. https://doi.org/10.1021/acs.inorgchem.0c02757.

(46) Estevenon, P.; Welcomme, E.; Szenknect, S.; Mesbah, A.; Moisy, P.; Poinssot, C.; Dacheux, N. Multiparametric Study of the Synthesis of $ThSiO_4$ under Hydrothermal Conditions. *Inorg. Chem.* **2018**, *57* (15), 9393–9402. https://doi.org/10.1021/acs.inorgchem.8b01390.

(47) Reynolds, H. S. Synthesis, Characterisation and Dissolution Studies of the Uranium Mineral Coffinite, Royal Melbourne Institute of Technology (RMIT) UNIVERSITY, 2013.

(48) Shuller-Nickles, L. C.; Ewing, R. C.; Becker, U. Atomistic Calculations of the Thermodynamic Properties of Mixing for Tetravalent Metal Dioxide Solid Solutions: $(Zr, Th, Ce)O_2$. *J. Solid State Chem.* **2013**, *197*, 550–559. https://doi.org/10.1016/j.jssc.2012.08.033.

(49) Aizenshtein, M.; Shvareva, T. Y.; Navrotsky, A. Thermochemistry of Lanthana- and Yttria-Doped Thoria. *J. Am. Ceram. Soc.* **2010**, *93* (12), 4142–4147. https://doi.org/10.1111/j.1551-2916.2010.04001.x.

(50) Subramani, T.; Navrotsky, A. Energetics of Formation and Disordering in Rare Earth Weberite RE_3TaO_7 Materials. *Inorg. Chem.* **2019**, *58* (23), 16126–16133. https://doi.org/10.1021/acs.inorgchem.9b02675.

(51) Finkeldei, S.; Kegler, P.; Kowalski, P. M.; Schreinemachers, C.; Brandt, F.; Bukaemskiy, A. A.; Vinograd, V. L.; Beridze, G.; Shelyug, A.; Navrotsky, A.; Bosbach, D. Composition Dependent Order-Disorder Transition in $Nd_xZr_{1-x}O_{2-0.5x}$ Pyrochlores: A Combined Structural, Calorimetric and Ab Initio Modeling Study. *Acta Mater.* **2017**, *125*, 166–176. https://doi.org/10.1016/j.actamat.2016.11.059.

(52) Horlait, D.; Claparède, L.; Clavier, N.; Szenknect, S.; Dacheux, N.; Ravaux, J.; Podor, R. Stability and Structural Evolution of $Ce^{IV}_{1-x}Ln^{III}_xO_{2-x/2}$ Solid Solutions: A Coupled μ-Raman/XRD Approach. *Inorg. Chem.* **2011**, *50* (15), 7150–7161. https://doi.org/10.1021/ic200751m.

(53) Shin, D. W.; Bridges, C. A.; Huq, A.; Paranthaman, M. P.; Manthiram, A. Role of Cation Ordering and Surface Segregation in High-Voltage Spinel $LiMn_{1.5}Ni_{0.5-x}M_xO_4$ (M = Cr, Fe, and Ga) Cathodes

for Lithium-Ion Batteries. *Chem. Mater.* **2012**, *24* (19), 3720–3731. https://doi.org/10.1021/cm301844w.

(54) Guo, X.; Szenknect, S.; Mesbah, A.; Clavier, N.; Poinssot, C.; Wu, D.; Xu, H.; Dacheux, N.; Ewing, R. C.; Navrotsky, A. Energetics of a Uranothorite ($Th_{1-x}U_x SiO_4$) Solid Solution. *Chem. Mater.* **2016**, *28* (19), 7117–7124. https://doi.org/10.1021/acs.chemmater.6b03346.

(55) Ushakov, S. V.; Helean, K. B.; Navrotsky, A.; Boatner, L. A. Thermochemistry of Rare-Earth Orthophosphates. *J. Mater. Res.* **2001**, *16* (9), 2623–2633. https://doi.org/10.1557/JMR.2001.0361.

(56) Mazeina, L.; Ushakov, S. V.; Navrotsky, A.; Boatner, L. A. Formation Enthalpy of $ThSiO_4$ and Enthalpy of the Thorite → Huttonite Phase Transition. *Geochim. Cosmochim. Acta* **2005**, *69* (19), 4675–4683. https://doi.org/10.1016/j.gca.2005.03.053.

(57) Risbud, A. S.; Helean, K. B.; Wilding, M. C.; Lu, P.; Navrotsky, A. Enthalpies of Formation of Lanthanide Oxyapatite Phases. *J. Mater. Res.* **2001**, *16* (10), 2780–2783. https://doi.org/10.1557/JMR.2001.0381.

(58) Zhang, Y.; Navrotsky, A. Thermochemistry of Rare-Earth Aluminate and Aluminosilicate Glasses. *J. Non. Cryst. Solids* **2004**, *341* (1–3), 141–151. https://doi.org/10.1016/j.jnoncrysol.2004.04.027.

(59) Popa, K.; Shvareva, T.; Mazeina, L.; Colineau, E.; Wastin, F.; Konings, R. J. M.; Navrotsky, A. Thermodynamic Properties of $CaTh(PO_4)_2$ Synthetic Cheralite. *Am. Mineral.* **2008**, *93* (8–9), 1356–1362. https://doi.org/10.2138/am.2008.2794.

(60) Robie, R.; Hemingway, B. S. *Thermodynamic Properties of Minerals and Related Substances at 298.15 K and 1 Bar (10^5 Pascals) Pressure and at Higher Temperatures*; 1995. https://doi.org/10.3133/b2131.

For Table of Contents Only
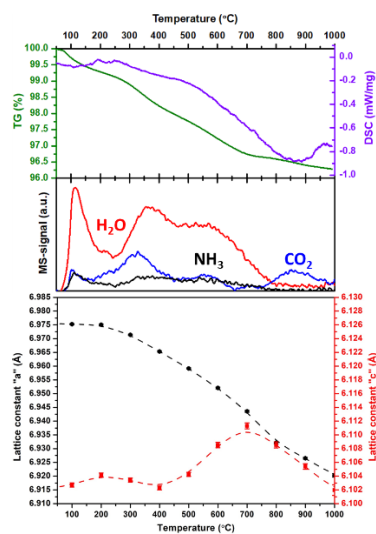
Synopsis

This paper is a complementary study to the one published in 2016 on thorium incorporation into zircon structure. It discusses effects of long-term storage and annealing on structure and thermodynamic properties of the mineral form doped with radioactive element. This is especially important in terms of the nuclear waste storage applications and understanding the durability of mineral structures in harsh environment of radioactivity.